surfaces

MDPI

Article

Design of Deterministic Microstructures as Substrate Pre-Treatment for CVD Diamond Coating

Richard Börner *, Michael Penzel, Thomas Junge and Andreas Schubert

Professorship Micromanufacturing Technology, Chemnitz University of Technology, Reichenhainer Str. 70, 09126 Chemnitz, Germany; michael.penzel@mb.tu-chemnitz.de (M.P.); thomas.junge@hrz.tu-chemnitz.de (T.J.); andreas.schubert@tu-chemnitz.de (A.S.)

* Correspondence: richard.boerner@mb.tu-chemnitz.de; Tel.: +49-3-715-313-3821

Received: 15 August 2019; Accepted: 11 September 2019; Published: 17 September 2019

Abstract: The coating of highly stressed components with chemical vapor deposition (CVD) diamond can extend their lifetime. In particular, the combination of steel substrates with diamond layers would find many applications in industrial production. However, there are some challenges, for example, the high mismatch in the thermal expansion between steel and diamond, which commonly leads to the delamination of the coating. Thus, a pre-treatment of the substrate surface is needed. Particle blasting has been established in some studies as a suitable process. However, apart from particle residues in the surface of the substrate, these surfaces have a stochastic character, which limits their reproducibility and modification options. This paper presents some instructions for the recording and derivation of defined properties of those surfaces. The conversion of characteristic surface features into quantitative process parameters could serve as the foundation for the manufacturing of deterministic microstructures, especially those produced by ultrasonic vibration superimposed machining. This should increase the reproducibility and the possibilities of the modification with regard to the structural shaping of the functional surface. The design was developed using both a kinematic surface simulation tool as well as a finite elements analysis for the cooling process of the coating–substrate–composite. A high accordance with real finished surfaces was achieved.

Keywords: coating; cooling simulation; functional surface; kinematical surface simulation; microstructure; surface analysis; thermal-induced residual stresses; ultrasonic vibration superimposed machining

1. Introduction

Increasing demands with regard to high sustainability, high resource efficiency, and low production costs are of priority in the industrial production of technical systems and components. As a result, coated surfaces have become more important, for example, in increasing the service life or improving the tribological behavior. In order to ensure sufficient adhesion of the coatings or coating systems, a suited modification of the surface is often advantageous. In this work, a surface functionalization to ensure the adhesion of chemical vapor deposition (CVD) diamond layers on steel substrates with a thickness above 2 µm is presented. This should be achieved by means of the derivation of the defined properties of stochastic surfaces and the subsequent conversion into quantitative process parameters as the basis for the generation of deterministic microstructures. Particular advantages include the reproducibility through a specific machining kinematics and tool geometry as well as the modifiability of the structures (e.g., depending on the layer thickness). Furthermore, there are some disadvantages in the strategy of particle blasting, which is currently used to obtain surfaces for CVD diamond application, like remaining as residues in the substrate surface. Associated with this, a complex machine system change could thus be replaced.

There are multiple studies that have examined the impact of the substrate surface microstructure on the adhesion strength of CVD diamond coatings with different substrate materials. The effect of the substrate roughness on the CVD diamond coating of Si3N4 specimens was reported by Amaral et al. [1]. The combination of different pre-treatments and seeding processes has led to the conclusion that surfaces roughened by plasma etching increase the layer adhesion of the CVD diamond coating due to "anchoring effects", whereby no closer information on the substrate roughness was given.

Singh et al. observed that the generation of a three-dimensional (3D) thermally and compositionally graded interface between diamond and the substrate material leads to improved adhesion of the CVD diamond film [2].

Under Wako et al., investigations were carried out regarding the layer adhesion of a CVD diamond coating on differently pre-treated molybdenum specimens (99.9% Mo) [3]. The molybdenum substrates were pre-treated by polishing and grinding to achieve both different roughness and anisotropic as well as isotropic surface microstructures. The substrates with the higher surface roughness showed a better layer adhesion. In addition, it was concluded that anisotropic structures let a crack pass only in one direction, while isotropic structures tended to exhibit circular layer delamination in a stress test.

Investigations on the influence of the surface roughness on the layer adhesion were also conducted under Xu et al. [4]. In this case, CVD diamond coatings were deposited on cemented carbide substrates with smooth as well as blasted surfaces using a Cr–CrN interlayer system. While the diamond coating of the specimens without any interlayer system flaked off directly during cooling, adherent CVD diamond with a thickness of approximately 9 µm was deposited on both with diffusion barriers. In a Rockwell-C indentation test, the diamond coating without surface pre-treatment showed significantly poorer attachment, which was shown through delamination at the interface to the interlayer. Thus, it can be concluded that increased surface roughness prior to CVD diamond coating enhances layer adhesion.

Gomez et al. found in cutting experiments that a preferential direction of the substrate roughness, resulting from the delivery state or the finishing of the cemented carbide inserts, had a negative impact on the subsequent adhesion of the CVD diamond layer (>20 µm) under mechanical stress [5].

By means of a more intensive mechanical interlocking and a mechanically graded transition from the substrate material into the CVD diamond coating, the compressive stresses in the transitional area can be significantly reduced when compared to a smoother substrate surface. This was found by Lee et al. in their investigations into the CVD diamond coating of laser induced micro-rough surfaces on cemented carbide substrates [6].

Grögler et al. generally concluded in numerous research studies that grit-blasting or grounding of the substrate surfaces are favored methods for CVD diamond coating adhesion in the case of deposition on titanium substrates [7–10]. The roughness of the pre-treated surfaces was between 0.5–1 µm (ground) and 3 µm (grit-blasted). They attributed this primarily to the effects of mechanical interlocking as well as elastic deformation, which leads to a reduction of thermally induced residual stresses.

Similar results in the CVD diamond coating of pure titanium were also be achieved by Lim et al. [11]. They concluded that a significant stress relaxation within the applied diamond layer could be effected by particle blasted and etching roughened substrate surfaces. This may be due to the fact that layer thickness and substrate roughness were of the same order of magnitude of about 3–5 µm. Here, the diamond layer was strong enough to prevent the contraction of the roughness peaks during cooling after the deposition process. As a result, only weak thermal compressive stresses arose within the layer.

In their review of CVD diamond deposition using various interlayers, Damm et al. also investigated the influence of a deterministic microstructure of the steel surface on the adhesion of the diamond layer [12]. They explained this by the formation of high thermally induced residual stresses within the layer, which led to spontaneous delamination at very flat substrate surfaces. For this reason, a substrate surface was examined, which was microstructured by laser-knurling. Thus, spontaneous delamination could be prevented, provided that suitable interlayers were used. This was attributed to the mechanical interlocking. However, no detailed information was given on the geometrical shape of the microstructure and its pre-design.

It becomes apparent that although there is some research on CVD diamond deposition on steel, which includes the influence of the substrate surface, however, little research has been done considering deterministic microstructures, and only methods with resulting stochastic surfaces have been used. Furthermore, the only investigation that dealt with a deterministic surface microstructure of a substrate did not provide any information as to which criteria the surface design was selected. Thus, there is a significant knowledge deficit, which should be systematically investigated.

Some researchers have already dealt with the areal characterization of (functional) surfaces, by applying, in particular, the standard DIN EN ISO 25178. Here, various property-related aspects of surfaces are considered and described by different parameter families.

- In their report, Seewig et al. introduced the 3D standard DIN EN ISO 25178, which claims to make the best possible use of the potential of topography evaluation [13]. The measuring chain, consisting of measurement data acquisition, measurement data preparation, and available characteristic operators, was described. The application limits of the ISO were also considered and alternative methods presented and compared with each other.
- In the book "Characterization of Areal Surface Texture", Leach recognized the growing need for three-dimensional (area) measurement and characterization techniques with the increasing need to control the functionality of surfaces [14]. Therefore, he presented an areal framework adopted by the international community. Unlike many other contributions that often address the measurement aspects, the book focused on the characterization techniques. The interpretation of the measured data was to decide importance in order to generate suitable (functional) information for a given task.
- In his PhD thesis, Hartmann concluded that conventional tolerance concepts for the specification and verification of geometric features (e.g., ISO GPS) are limited for applications in the micro- and nanometer range [15]. This can be explained by the insufficient mapping of functional relationships between geometrical and non-geometrical features, which significantly influence the functionality of a workpiece. In the design-oriented verification process, only standardized parameters are recorded and evaluated independently of each other. A holistic, multi-dimensional assessment of acquired measurement data with respect to a function-oriented conformity decision is missing. In his work, Hartmann provides an approach for solving this deficiency by means of a transferable method for the predicative assessment of the degree of expected functionality of structured workpiece surfaces. The models are based on real surface measurement data.

Although these studies deal in detail with the evaluation and interpretation of 3D surface measurement, no approach to derive deterministic properties from stochastic surfaces has yet been found. The design and manufacture of so-called bionic structures is also subject to a different process, as natural deterministic surface microstructures serve as a template for the generation of technical functional surfaces, for example, the sharkskin or lotus blossom effect.

Therefore, the main objective of this work was the characterization of blasted surfaces by means of suitably selected properties and parameters as well as a surface design based on derived geometrical features. Thus, the effect of individually influencing variables such as, for example, the layer thickness or the structural distance, can be determined on the thermally induced residual stresses in the corresponding deterministic microstructures. This was carried out both simulatively by a finite elements analysis cooling model for the two-dimensional case as well as experimentally after conversion into real 3D surfaces. The derived surface requirements were converted into a kinematic simulation taking into account production-realistic conditions. Finally, the surfaces were representatively manufactured by means of an ultrasonic vibration superimposed machining (UVSM).

In conclusion, the general possibility of producing deterministic structures with properties similar to those of the blasted ones may be considered, for example, with deviations resulting from tool wear.

2. Materials and Methods

2.1. Cooling Simulation Model

During the coating process, both the steel and the newly formed diamond layer reach typical temperatures above 900 °C. In the CVD diamond coating of steel in particular, a major challenge is that both materials have very different thermal expansion coefficients. On cooling from the coating temperature to room temperature, different strains and especially strong residual compressive stresses occur in the diamond layer, which frequently lead to spontaneous buckling or spalling of the diamond layer. The investigations were carried out by means of the cooling simulation (CS) using the software COMSOL Multiphysics® (COMSOL Group, Stockholm, Sweden). They aim for a defined surface finish, which can reduce residual stresses in the coating and/or distribute them more favorably. Figure 1 shows the 2D model geometry, which is an example of a profile section in surfaces produced by ultrasonic vibration superimposed machining. The base of the model consists of a 1 mm high by 0.5 mm wide steel surface, which is characterized by a sinusoidal top edge. Using a second formula with an amplitude of $A_2 \leq A_1$, the contour mapping behavior of the diamond monolayer can be varied, analogous to a real CVD coating process. The distance between the peaks of the two functions defines the thickness, D. This ensures that a minimum thickness in the vertical direction is maintained. It was considered in the simulations with 2 µm and 5 µm. The base was assigned as a stainless austenitic steel (X46Cr13). The coating layer formed from the two sine functions was defined with the material diamond. To evaluate the resulting residual stress, a linear-elastic model was chosen for both areas, which included the consideration of the material parameters, Young modulus and Poisson ratio. The values for those parameters were taken from the COMSOL material library. The interface between the layer and substrate was defined by a fixed connection, which can be seen by the meshing of the interface, which is also represented in Figure 1. In the 2D simulation, the current state of the stress distribution after the cooling process from 900 °C to 20 °C was calculated. A determination of the evaluation area was made before the model calculation, so that critical marginal areas could be ignored.

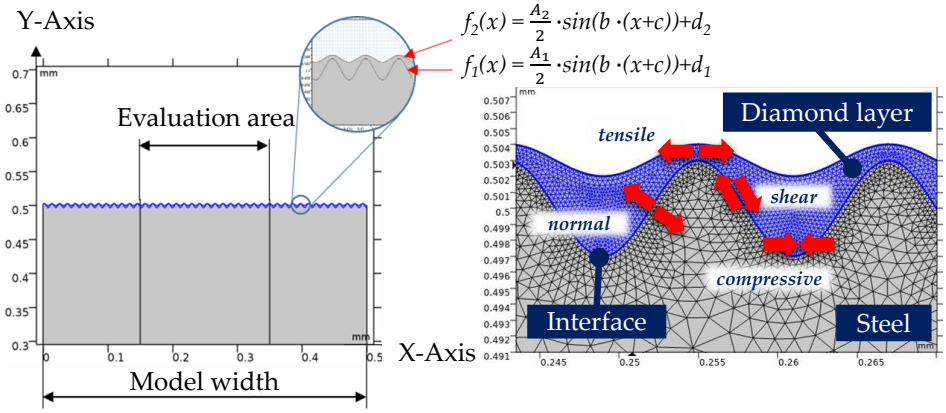

Figure 1. Example of a 2D geometry of the cooling simulation model and an illustration of the mesh distribution and the considered residual stresses.

The physical modules "Solid Mechanics" and "Heat Transport in Solids" were used to set up different models. The whole condition was defined with the condition "solid" and "linear elastic material". The conditions "Free" and "Heat Flux" were chosen as the boundary conditions. The boundary condition "Free" was considered a standard boundary condition and realizes that no restrictions and loads act on the boundary layer. "Heat Flux" realizes the heat flow to the outside and overwrites the standard setting "Thermal insulation". The meshing is done with triangular elements to allow easy shifting of the mesh in each direction. It was defined that the mesh elements in the diamond area could not assume a size of >0.3 µm. The maximum values of the principle stresses (compression and tension) as well as the normal stresses and shear stresses on the interface were evaluated.

The cooling simulation serves to derive trends and are therefore initially created as a simplified model. This neglects some of the real conditions and circumstances presented below:

- a chemically necessary intermediate layer including its geometric and material-specific properties;
- the variability of the thermal expansion coefficient of the materials considered in relation to the temperature;
- the phase transformation of the steel material as well as its associated volume change;
- the cooling rate; and
- the grain size of the diamond layer: micro or nano crystalline.

2.2. Kinematic Surface Simulation Model

The kinematic surface simulation model was done in the software MATLAB R2017a (The MathWorks, Inc., Natick, MA, USA) and first introduced in [16]. This dexel-model is based on the Boolean intersection of the tool and workpiece along the tool trajectory to simulate the resulting surface microstructure. Therefore, it represents a kinematic approach that regards no physical effects such as burr formation, chipping or force and temperature influences. In comparison, this modeling approach was further improved in terms of its simulation performance and operability. The resolution has a major influence on the simulation efficiency. While the spatial resolution of the workpiece and tool are fixed regarding a good ratio of simulation time and image accuracy of the surface structure (distance of neighboring dexels in X and Y direction ΔXY: workpiece 1 µm; tool 0.5 µm), the temporal resolution depends on the setting of process parameters. Hence, the simulation model was extended by the automatic calculation of the least necessary temporal resolution that was calculated by the number of intersections per period N and an ultrasonic frequency of approx. f_{US} = 19 kHz:

$$t_{Sim} = 1/(N \cdot f_{US}). \tag{1}$$

The distance of two neighboring points should be at least as high as the distance between two neighboring workpiece dexels ΔXY. Therefore, it depends on the relationship between the wavelength of the oscillation λ and the spatial workpiece resolution that can be represented by the following formula:

$$N = \lambda/\Delta XY = D_{tool} \cdot \pi \cdot n_{tool}/(f_{US} \cdot \Delta XY) \tag{2}$$

Since a sine wave needs a minimal number of points for an adequate representation, the minimal number of intersection points per period were fixed at 20 for small wavelengths (<20 µm). Furthermore, the simulation efficiency was increased by a simplification of the tool representation. Instead of using a complex three dimensional model with a high number of dexel points, the tool is only represented by a contour line along the minor and major cutting edge. Therefore, the number of tool points and the simulation time are significantly reduced while obtaining the same simulation results. For efficiency reasons, the tool contour height should not be higher than the maximum possible structure height Rz_{clac}, which is composed of the kinematical roughness and the vibration-induced microstructure. The kinematical roughness is caused by the offset of the cutting edge geometry in the direction of the feed, while the microstructure in the direction of the cutting speed results from the combination of the oscillating and cutting motion. Therefore, Rz_{calc} can be calculated by the feed per tooth f_z, the tool cutting edge angles of the major as well as the minor cutting edge and the vibration amplitude A_{US} (peak–peak).

$$Rz_{calc} = \frac{tan(\kappa) \cdot tan(\kappa') \cdot f_z}{tan(\kappa) + tan(\kappa')} + A_{US} \tag{3}$$

The height of the resulting microstructure can still be smaller, but never larger due to the overlapping effects of the kinematic roughness and the vibration-induced microstructure. Despite the tool abstraction, the model was still sufficient to adequately represent the tool and the simulated surface. To translate the simulation results into reality, the possible case of an intersection of the flank

face with the surface structure had to be considered (compared to [16]). The improvement of the simulation efficiency facilitates the conducting of comprehensive studies on the influence of process parameters on the structural characteristic of the surface. In addition, a new tool import interface was included that enables the direct import of STL tool geometries. Consequently, it is possible to simulate surface structures with 3D measured tools. The measured data points have to be transformed into STL data with an adequate resolution by means of CAD software before importing them into the simulation model.

For a better evaluation and assurance of the reproducibility of the surface structures, the model was expanded by an analysis tool for the resulting deterministic microstructure. It enables the calculation of a set of structural parameters that represent different characteristics of ultrasonic vibration superimposed machined (UVSM) surfaces. Contrariwise, it is also possible to manipulate the structure parameters and calculate the required change of machining parameters. Hereafter, the most important structural parameters regarding the subsequent surface design are explained:

AR describes the aspect ratio in the direction of the cutting speed.

$$AR = A_{US}/\lambda \tag{4}$$

A_{fz} describes the aspect ratio in the direction of the feed velocity. Therefore, it determines if the kinematic roughness or the vibration-induced microstructure is more dominant.

$$A_{fz} = A_{US}/f_z \tag{5}$$

$R_{r\varepsilon}$ describes the ratio of the corner radius in relation to the wavelength of the oscillation. It characterizes the shape and extension of the valleys of the surface microstructure.

$$R_{r\varepsilon} = 2{\cdot}r_\varepsilon/\lambda \tag{6}$$

R_{fz} describes the ratio of the feed per tooth in relation to the wavelength of the oscillation. Therefore, it has an influence on the number of structural elements in the the feed and the cutting direction.

$$R_{fz} = f_z/\lambda \tag{7}$$

R_λ describes the ratio of the ultrasonic frequency in relation to the rotational speed ("wavelength ratio"). Thus, it rates the structural offset in the direction of the cutting speed between two successive feed paths. If the result is an integer value, the offset between the structures is zero. Otherwise, there is an offset of half the wavelength if the result is an odd multiple of 0.5. Since only the decimal place is relevant, the value before the comma is replaced by an "X".

$$R_\lambda = f_{US}/n_{tool} \tag{8}$$

The kinematic simulation model was applied to verify the influence of the introduced structural parameters. $R_{r\varepsilon}$, R_{fz}, and R_λ were varied separately by the adjustment of the machining parameters n_{tool} and f_z as well as the corner radius of the tool r_ε. These varied parameters as well as the constant input parameters are shown in Tables 1 and 2. The resulting simulation surfaces are qualitatively compared in Tables 3 and 4 for two different wavelength ratios R_λ. It should be noted that to emphasize the surface patterns, an equal scaling of the color values as well as the indication of the respective elevation scale was waived, since these are partly very different. However, this has no relevance to the presentation of the facts. The size of the analyzed area was 200×100 µm^2.

Table 1. Constant simulation parameters for the verification of the structural parameters.

Constant Parameter	$r_{tool,\,eff}$ [mm]	κ [°]	κ′ [°]	A_{US} [µm]	f_{US} [kHz]
value	9	45	45	4	19

Table 2. Variable simulation parameters for the verification of the structural parameters.

Variable Parameter	n_{tool} [min^{-1}]	f_z [µm]	r_ε [µm]
value	523.056/523.176	12.97/25.95/51.89	6.49/12.97/25.95

Table 3. Simulated surface structures with a wavelength ratio with an odd multiple of 0.5.

	R_λ = X.5		
R_{fz}	$R_{r\varepsilon}$ = 0.5	$R_{r\varepsilon}$ = 1	$R_{r\varepsilon}$ = 2
0.5	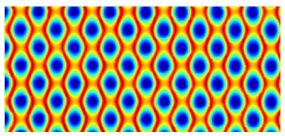	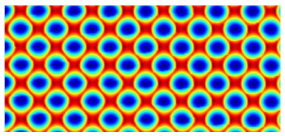	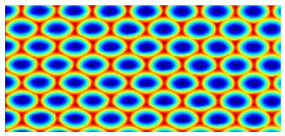
1	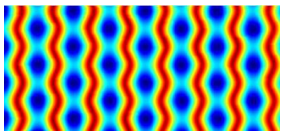	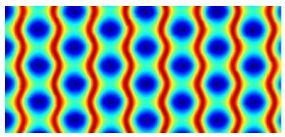	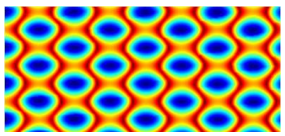
2	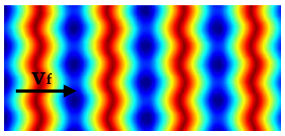	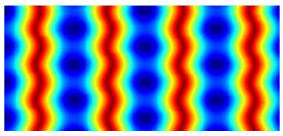	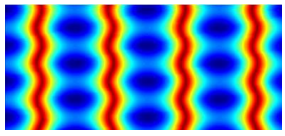

Table 4. Simulated surface structures with an integer wavelength ratio.

	R_λ = X.0		
R_{fz}	$R_{r\varepsilon}$ = 0.5	$R_{r\varepsilon}$ = 1	$R_{r\varepsilon}$ = 2
0.5	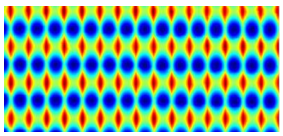	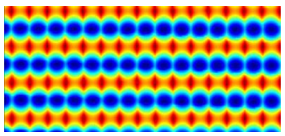	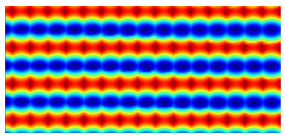
1	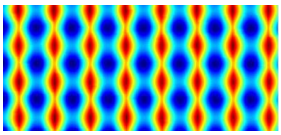	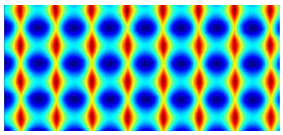	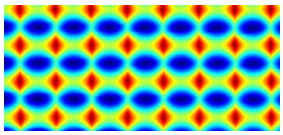
2	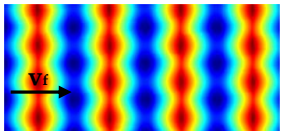	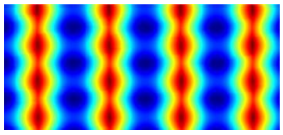	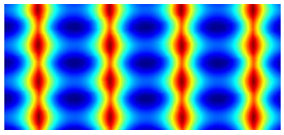

As can be seen in the tables, the rise of R_{fz} led to a reduction of A_{fz}. Hence, the kinematical roughness became more dominant in comparison to the vibration-induced microstructure. Furthermore, the number of structural elements (valleys) in the feed direction decreased by half with the three-stage increase of R_{fz} by twice. The variation of the wavelength ratio over the speed occurs in the decimal range. Therefore, there are virtually no changes of the wavelength and of the number of valleys in the cutting direction.

A comparison of Tables 3 and 4 shows that R_λ has a major influence on the surface isotropy. An odd multiple of 0.5 more likely results in plateau-like surfaces with a staggered arrangement of

valleys at low feeds, because the minor cutting edge cuts off the peaks of the previous feed path. In contrast, an integer value of R_λ led to anisotropic linear peak-shaped structural elements at low feeds. With higher feeds, the surface was dominated by ridges in the direction of the cutting speed. Thus, the change of R_λ only affects the shape of these structural elements.

The simulations show the influence of R_ε on the shape of the valleys of the microstructure. With a value smaller than 1, the valleys were stretched in the direction of the cutting speed. A value of (nearly) 1 led to circular valleys, and if $R_\varepsilon > 1$, they were stretched vertically in the direction of the cutting speed. Moreover, the larger the corner radius in relation to the feed, the greater its influence on the structural shape. A uniform ratio of the doubled corner radius and the wavelength of the microstructure causes a circular shape of the valleys instead.

2.3. Ultrasonic Vibration Superimposed Machining

The generation of the microstructures on the machined surface in ultrasonic vibration superimposed milling with oscillating excitation in the direction of the tool axis (perpendicular to the specimen surface) has already been described in [16,17]. Additionally, in the present work, the vibration was realized by an oscillating specimen. In order to reduce the influence of the curvature of the path on the surface, a single-edged insert cutter with a diameter of 18 mm was used. Moreover, due to the deterministic properties of the UVSM microstructures, a relatively small measurement area was considered as sufficient. The used ultrasonic generator allows the use of a fixed oscillation frequency, so that the adjustment of R_{fz} (described in Section 2.2) is possible in principle. Despite the fact that the material of the particle blasted reference specimens initially considered was a steel material, the machining tests were carried out in brass (CuZn40Al2). It was expected that due to the generally better machinability, a higher accuracy to the simulated microstructures could be achieved.

2.4. Surface Measurement and Analysis

The 3D data of the generated surfaces were gathered using an optical laser scanning microscope of the type Keyence VK-9700 (Keyence Corporation, Osaka, Japan). The surface analysis was carried out taking into account the specifications from DIN EN ISO 25178-2. For this purpose, the surface analysis and evaluation software MountainsMap® 7.4 (Digitial Surf, Besançon, France) was used. In addition, the VK-Analyzer software (Keyence) was used to display images of the tool wear.

3. Results

3.1. Surface Derivation

The derivation of defined properties of stochastic surfaces as well as the conversion into quantitative process parameters as the basis for the generation of deterministic microstructures are described below. As described in the state of the art, particulate blasting especially represents a proven form of substrate surface pre-treatment for CVD diamond coating on steel materials. Accordingly, stochastic reference surfaces were prepared on X46Cr13 (austenitic steel) with this method using SiC grain. The resulting surface is shown in Figure 2 and was characterized metrologically. For the optical surface measurement with the 3D laser scanning microscope, a magnification factor of 50 was used. For the determination of selected surface characteristics according to DIN EN ISO 25178, the surface data were evaluated by means of the MountainsMap 7.4 software. The operation "Resample" was used to provide all surfaces with an equal resolution in the X as well as in the Y direction of 0.5 µm to analyze the surface magnification. After extracting a square area with a side of 0.5 mm, the profile was aligned using the least squares subtraction method. In addition, the surface was filtered using a robust Gaussian filter with a size of 200 µm. In order to reduce the influence of outliers (e.g., residuals or pores), three areas with the size 200 × 200 µm^2 (according to DIN EN ISO 25178-3) without visible surface defects were selected from the 500 × 500 µm^2 measuring field.

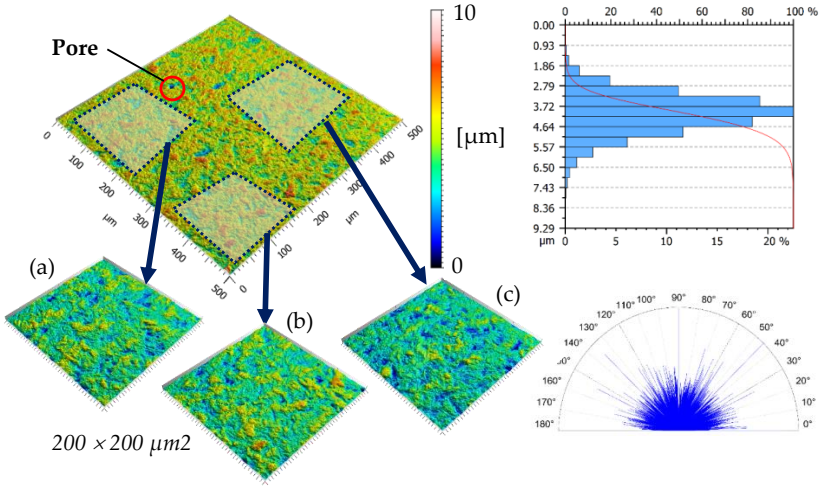

Figure 2. Surface selection (**a**–**c**) as well as the Abbott and material ratio curve (above) and isotropy diagram (below) of the large measurement field.

The values of the considered parameters were averaged and thus formed the reference values. In addition, the value of the parameter *Sz*, which is used as a filter parameter for the motif analysis initially at 5%, approached the value of the more robust parameter *S10z* through this procedure. This parameter expresses the mean value of the five highest and five deepest points of a considered measuring field and is nearly comparable to the parameter *Rz* in the 2D profile measurement.

In addition, Figure 2 shows the Abbott and material ratio curve as well as the isotropy diagram, valid for the large measurement field. The "S-shaped" course of the Abbott curve indicates that the particle blasted surfaces were marked by a nearly uniform material distribution with a slight shift of the parts toward the tips. Furthermore, no preferential direction could be recognized, so the surface texture could be described as isotropic. This was confirmed by the subsequent evaluation of the surface parameters. A geometric specification of the profile could be created for the deterministic microstructure to be generated by using surface parameters. For this purpose, typical parameters were selected from various parameter families, which characterized the surface of the reference as well as the simulated surfaces and those produced by UVSM in a suitable way: Spatial parameter (*Str*); hybrid parameter (*Sdq, Sdr*); functional parameter (*Sk, Spk, Svk, Smr1, Smr2*); and feature parameter (*S10z*). Additionally, the results from the motif analysis were considered. Here, the motif distance as well as the number of neighbors were averaged. An example for the measuring field (c) is represented in Figure 3.

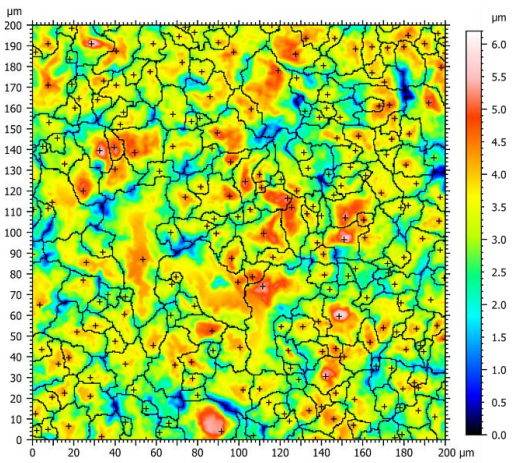

Figure 3. Motif analysis of field see Figure 2c with marking of the highest peak in each element.

Table 5. Overview of the quantitative analysis of the 200 × 200 µm^2 areas.

Surface Parameter	Value (a/b/c)	Average
S10z [µm]	4.46/5.00/5.71	5.1
Sdr in %	16.1/16.9/16.8	16.6
Str in %	88/83/84	85
Sdq	0.62/0.64/0.64	0.63
Abbott curve		
- *Sk* [µm]	2.04/1.93/1.95	1.97
- *Spk* [µm]	0.62/0.61/0.75	0.66
- *Svk* [µm]	0.81/0.82/0.87	0.83
- *Smr1* in %	8.32/9.79/9.83	9.3
- *Smr2* in %	89.6/88.4/89.1	89
Averaged motif distance [µm]	15.2/15.0/17.1	15.8
Number of neighbors	5.33/5.47/5.35	5.4

For the design and subsequent manufacturing of these microstructures, the process parameters for the UVSM had to be derived from these specifications. As mentioned in Section 2.3, the amplitude and the frequency of the oscillating system as well as the machining parameters cutting speed and feed define the microstructure, whereby the feed can represent a direct geometrical size (distance in the feed direction), while the wavelength is defined via the cutting speed or the spindle rotation, respectively, under the condition of a constant vibration frequency. With a sufficiently large tool diameter and a much smaller measuring area considered, this specifies the orthogonal distances to the feed direction. Furthermore, the profile height is adjusted by means of the amplitude, but in consideration of the cutting geometry and feed resulting kinematic roughness. The variation of the rotational speed in the single-digit range enables to adjust the displacement of the microstructure in the feed direction ($\rightarrow R_{fz}$) as well as the distribution of peaks or valleys, which is described in Section 2.2. The determined characteristic values taken from Table 5 led to the following specification:

- Profile height: approx. 5 µm
- Distance between motifs: approx. 15–16 µm
- Number of motif neighbors: 5–6
- Furthermore, the following features are desired:

  an isotropic surface or a distribution of the microstructures without preferential direction, respectively;
  an even material distribution; and
  more steep than flat microstructures.

3.2. Results of the Cooling Simulation

The reference represents an ideal smooth surface (Figure 4). It is noticeable that the maximum compressive stresses were lowest under these conditions. However, they prevailed in each area of the considered layer section, which, according to experience, leads to delamination of the diamond layer in this magnitude. As also seen in Figure 4, the neglected area on the lateral border is visible. The value of the maximum compressive stress $\sigma_{min} = -6.2$ GPa corresponds to the order of magnitude previously calculated analytically in some literature sources [6,18].

It is hypothesized that microstructuring ensures a "heterogenization" of the compressive stresses with the formation of local peaks, resulting in a significant relaxation in the remaining area of the diamond layer. This approach enables stress relaxation by elastic pre-bending of the actually brittle diamond layer.

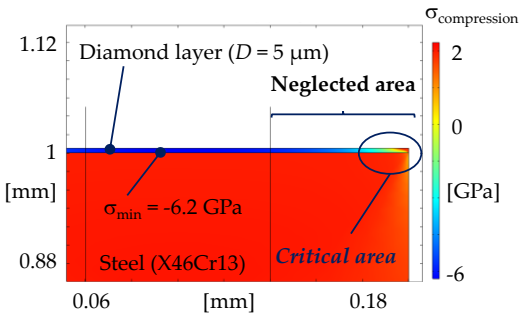

Figure 4. Smooth reference surface with compressive stresses in false colors.

For the extensive characterization of the relationships between the input parameters and the target values, particularly low residual stresses (e.g., by calculating correlations), various parameters were introduced that describe the geometric relationships between the microstructure and diamond layer. These are, including their calculation, shown in Table 6.

Table 6. Introduced relationships.

Designation	Calculation	Description
AR	A_1/λ	Aspect ratio
CR	A_2/A_1	Contour mapping ratio
LR	D/A_1	Layer thickness ratio
MR	Terms (9–11)	Material ratio

The aspect ratio *AR* describes whether the microstructure of the substrate is rather shortwave or longwave. The contour mapping ratio *CR* describes how contour-accurate the diamond layer is deposited. The layer thickness ratio *LR* provides information about the ratio of the layer thickness to the profile height of the microstructure of the substrate. The material ratio *MR* compares the material proportions between the substrate and diamond layer over a defined range of one period ($\lambda = 2\pi$) and is calculated by Equations (9)–(11), and illustrated in Figure 5.

$$MR = \frac{M1}{M2 - M1} \tag{9}$$

$$M1 = \int_0^{2\pi} \left(A_1 \cdot \sin\left(\frac{2\pi}{\lambda} \cdot x\right) + \frac{A_1}{2} \right) dx \tag{10}$$

$$M2 = \int_0^{2\pi} \left(A_2 \cdot \sin\left(\frac{2\pi}{\lambda} \cdot x\right) + \left(A_1 + D - \frac{A_2}{2} \right) dx \right. \tag{11}$$

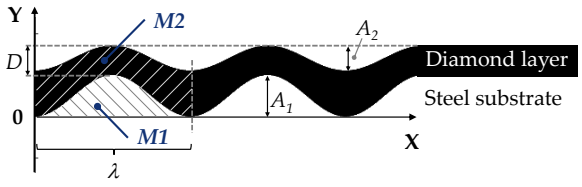

Figure 5. Schematic illustration of the material ratio *MR*.

The input parameters for the cooling simulation are shown in Table 7. Regarding the layer thickness, which is given in many research terms as the maximum possible adherent, 2 µm was chosen as well as 5 µm. The latter represents a technological challenge. Furthermore, in addition to the structural height derived in Section 3.1, further amplitudes (A_1, peak–peak) were investigated, since this, in particular, depending on the thickness of the layer, is expected to have a major influence on the

resulting layer tensions. The layer amplitude A_2 covered the whole range of the contour mapping ratio for each amplitude, from true-to-contour ($A_1 = A_2$) to nearly plane-like flat surface ($A_2 = 0$ or 1 µm, respectively), and was varied in steps of 2 µm. The structural distances according to the motif analysis were adjusted via the wavelength λ of the sine function. However, in order to specify these with respect to the substrate amplitude A_1, fixed aspect ratios (AR) were selected from the height to width or distance of the structural elements, respectively. The wavelengths for the respective substrate amplitudes can thus be calculated. The determination of the aspect ratio started at $AR = 1/3$ in response to the derived requirement (height: 5 µm, distance: 15 µm) and was reduced by a further three levels, since a larger AR cannot be produced technologically with the described method (UVSM). The entire matrix of input parameters and for each combination the results of the four residual stresses considered are shown in Appendix A. In some cases, there were no tensile stresses in the evaluation area, so the corresponding cells are empty.

Table 7. Input parameters of the cooling simulation.

Parameter	Unit	Value
Substrate amplitude A_1	[µm]	2; 3; 4; 5; 6
Layer amplitude A_2	[µm]	A_1-2*n ($0 \leq n \leq A_1/2$)
Layer thickness D	[µm]	2; 5
Aspect ratio AR	-	1/3; 1/4; 1/5; 16

Since, in the state of the art, most of the thermally induced compressive stresses within the diamond layer are detected as the main cause of layer delamination, these are examined in more detail below. However, an abstraction of the results is useful, because the absolute values of the residual stresses are only approximately of relevance to the evaluation of the microstructuring due to the above-mentioned simplifications of the simulation model. Thus, Table 8 shows the absolute difference of the compressive stresses $\Delta\sigma_{compression}$, which means that the absolute minimum compression stress $|\sigma_{min}|$ has been subtracted from each absolute value. Therefore, it becomes possible to evaluate optical trends through the colored marking as well as the absolute differences within the examined parameter field, which should have a higher validity. Green colours thus represent the smallest compressive stresses, red the largest.

Table 8. Illustration of the absolute difference of the compressive stresses $\Delta\sigma_{compression}$ in GPa within the diamond layer with $|\sigma_{min}| = 7.6$ GPa.

Thickness Diamond Layer		***D* = 2 µm**				***D* = 5 µm**			
A_1	A_2	**Aspect Ratio *AR* (A_1/λ)**							
[µm]		**1/3**	**1/4**	**1/5**	**1/6**	**1/3**	**1/4**	**1/5**	**1/6**
2	0	5.23	4.09	3.28	2.68	4.13	3.01	2.23	1.68
2	2	6.42	4.84	3.80	3.00	8.87	7.07	5.82	4.84
3	1	5.34	3.86	2.91	2.29	4.94	3.79	2.93	2.26
3	3	3.05	2.45	1.92	1.51	8.84	6.62	5.11	4.04
4	0	5.57	4.39	3.61	3.13	4.30	3.20	2.41	1.84
4	2	3.38	2.38	1.76	1.39	5.22	3.77	2.70	1.93
4	4	1.40	1.21	0.98	0.74	7.32	5.26	3.90	2.97
5	1	4.81	3.67	3.01	2.62	4.66	3.36	2.43	1.75
5	3	1.75	1.24	0.95	0.80	4.70	3.14	2.09	1.35
5	5	0.51	0.54	0.45	0.30	5.49	3.90	2.85	2.06
6	0	5.49	4.48	3.88	3.53	4.16	3.04	2.23	1.65
6	2	3.57	2.80	2.37	2.15	4.56	3.11	2.12	1.43
6	4	0.67	0.51	0.44	0.43	3.97	2.35	1.41	0.77
6	6	0.00	0.14	0.11	0.02	3.96	2.84	2.01	1.37

In order to quantitatively characterize the influence of the direct input parameters as well as the established conditions on all of the considered residual stresses, the result values were compared with

the corresponding matrices. The correlation function is suitable for this. The resulting correlation coefficient can be used to determine the relationship between the respective input parameters. As far as the correlation coefficient is closer to +1 or −1, it indicates a positive (+1) or negative (−1) correlation between the parameters. Positive correlation means that the values of one matrix also increase as the values in the other matrix increase. A correlation coefficient closer to zero indicates no or only a weak correlation. The equation for calculating a correlation coefficient is:

$$Korrel(X,Y) = \frac{\sum(x-\overline{x})(y-\overline{y})}{\sqrt{(\sum(x-\overline{x})^2\sum(y-\overline{y})^2}} \tag{12}$$

In this case, $\overline{x}$ and $\overline{y}$ represent the sample mean values of the compared matrices. For a lucid presentation of the results of the correlation calculation, a net diagram was chosen, which indicates the correlation value both with respect to the input parameters and to the introduced relationships. In this way, the correlation factors of a residual stress become visible in comparison to the others as well as the similarities and differences.

As shown in Figure 6, the colored curves indicate that the four varied input parameters in different areas of the test matrix have a different influence on the expression of the compressive stresses. For example, high substrate as well as layer amplitudes appear to be favorable with low layer thicknesses, while the structural distances there, expressed by the aspect ratio, hardly have any influence. This finding supports the hypothesis of elastic stress relaxation, since in the case of a high contour mapping accuracy and in relation to the layer thickness large amplitudes, pre-bending effects are most likely to be expected. At lower amplitudes and, in particular, larger layer thickness, this is already different.

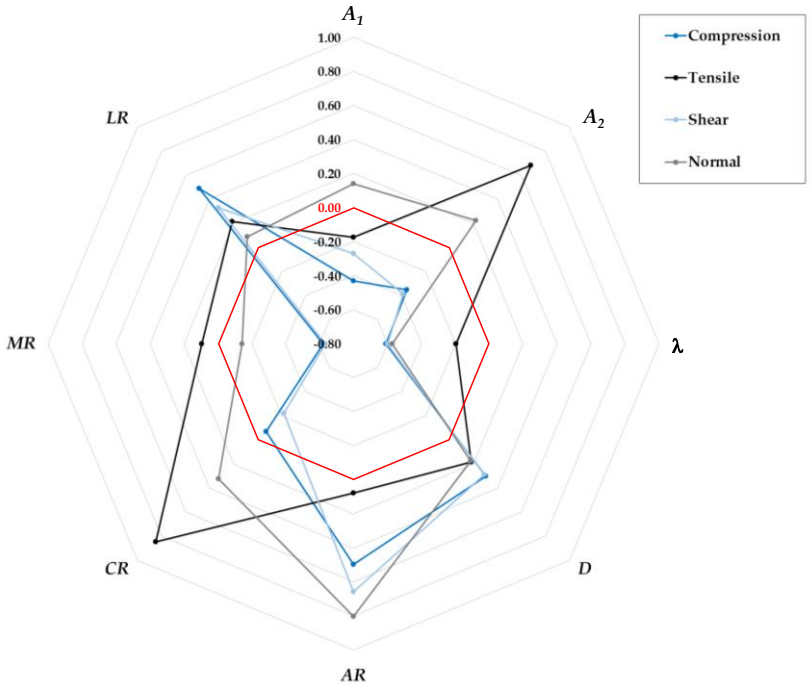

Figure 6. Diagram of correlations between the input parameters, introduced ratios, and target sizes (residual stresses).

Further more, there were some dominant (≥|0.5|) relationships. In particular, the high positive correlation between the residual stresses and the aspect ratio *AR* should be emphasized as well as being mostly accompanied with a high negative correlation to the structural distances. This means that the influence of the amplitude A_1 on the resulting stresses was significantly lower than assumed.

In addition, the compressive and shear stress had a high negative correlation with the material ratio. This behavior was substantiated by a correlation factor of 0.87 between these two stress factors. The tensile stresses were the only residual stresses with a relatively high correlation factor to the amplitude of the diamond layer. This is mainly due to the characteristics of the distribution of principle stresses within the layer, which is clarified in Figure 6. However, it should be noted that the largest differences between the maximum and minimum values for tensile, shear, and normal stresses were above 2 GPa for values between 0.2 GPa and 2.23 GP, while, as shown in Table 8, the largest differences in compressive stresses were at 8.87 for values between −7.6 GPa and −16.47 GPa. However, the correlation factors did not take these ratios into account. In a visual comparison of different parameter combinations, therefore, the differences in tensile stresses were only slightly noticeable. Furthermore, the layer thickness did not have a significant influence on the magnitude of the residual stresses in the examined parameter field, considering the correlation factors with D. However, this can be explained by the comparatively small number of input values for the layer thickness in relation to the total number of all combinations. Here, the correlation factor was less significant, which is also reflected in Table 8.

The amounts of the compressive stresses decrease with increasing amplitude A_1; in addition, with a constant A_1, the amounts of the compressive stress decrease with increasing amplitude A_2. However, with a small layer thickness and large amplitudes A_1 as well as A_2, a high contour mapping ratio is achieved, which is for many technological applications rather undesirable/unfavorable as there is only a small contribution as well as an uneven surface. Furthermore, the influence of the AR is greater with thicker layers or even with small amplitudes A_1: if the AR decreases due to increasing λ, the compressive stresses are reduced. At the same time, a "homogenization" of the compressive stresses occurs, which is shown in Figure 7. This means that at $A_1 = 0$, the minimum is reached. However, this case is also unfavorable in the reality as described above.

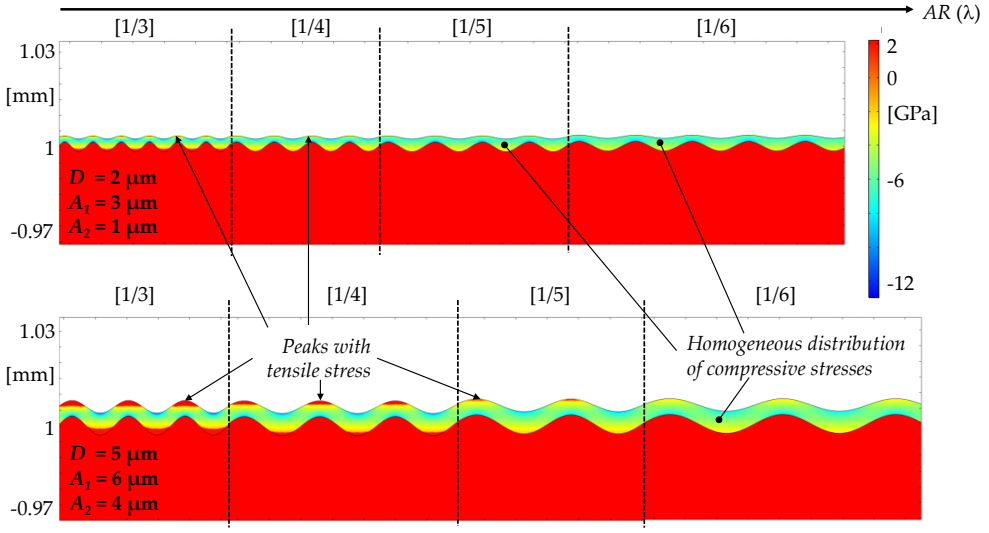

Figure 7. Effects of the variation of the aspect ratio on the distribution of the main residual stresses within the layer for two different cases (above: A_1 = 3 µm, A_2 = 1 µm, D = 2 µm; below: A_1 = 6 µm, A_2 = 4 µm, D = 5 µm).

In Figure 7, two parameter combinations of the parameters D, A_1, and A_2 are shown, each case for all four considered aspect ratios. The material ratio was the same in all cases (MR = 0.5). Despite the different input parameters, the principle stresses showed similar trends. As the wavelength increased, which means a decreasing AR, both the compressive stresses decreased in magnitude as well as the tensile stresses, which corresponded to the previously established hypothesis. In the upper shown case, for AR = 1/5 and AR = 1/6 as well as the lower case for AR = 1/16, they even did not exist. It can also be seen that with an increasing AR, there were still areas with tensile stresses in both the peaks

and in the valleys of the layers. The latter evidently built up faster with an increasing wavelength than the tensile stresses in the peaks. A reason could be the different extent of the radii of curvature within the layer at a $CR < 1$, which means $A_2 < A_1$. This conclusion is supported by the comparatively high correlation factor between *CR* and the tensile stresses. Although there are clearly different layer amplitudes A_2, the differences in the magnitude tensile stresses were comparatively small. In addition, it could be stated that *LR* as well as mostly *CR* had only little (direct) influence on the residual stresses.

3.3. Surface Simulation and Manufacturing via UVSM

Based on the derived geometric requirement profile, a surface was designed, which initially only indicated the "profile height" of 5 µm, which was set by the US amplitude (peak–peak), and the "structural distances" of 15 µm, both in the direction of the feed as well as the cutting speed, respectively. In addition, a wavelength ratio of X.0 was initially selected to obtain a majority "peak-shaped" surface microstructure. An geometrically ideal corner radius smaller than the feed was chosen (10 µm) to avoid any influence on the microstructure. The ultrasonic vibration frequency was set to 19 kHz. The simulated surface is shown in Figure 8. As can be seen, the *Sz* value of the simulated surface, which is visible at the height range of the color bar, was higher than 7 µm and thus more than the set ultrasonic amplitude. This was due to the superimposition effects of the kinematic roughness, which were explained in Section 2.2.

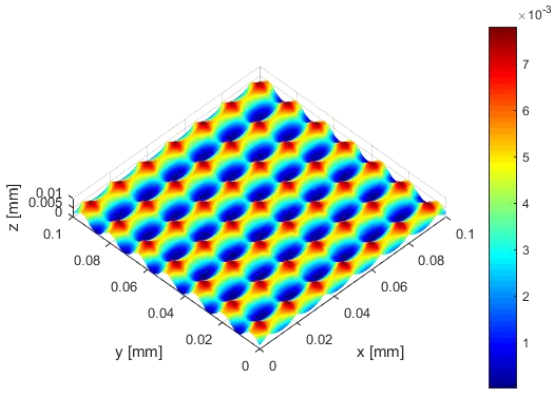

Figure 8. Simulated surface with derived properties: A_{US} = 5 µm; f_z = 15 µm; λ = 15 µm; r_ε = 10 µm; R_λ = 0.

However, the hereby presented aspect ratio of AR = 1/3 is not technologically achievable. Earlier trials on the UVSM showed that the limit is around AR_{max} = 1/4, since this is associated with an extremely large clearance angle as well as a lower wedge angle, and these geometrical tool specificities are limited in the manufacturing process of cutting tools. Furthermore, decreasing the aspect ratio corresponds to the recommendations from the cooling simulation. Thus, an adjustment regarding the technological reality as well as the findings of the cooling simulation was necessary. Two different approaches to the structural design were made, followed by a simulative implementation, and subsequent manufacturing. This is stepwise described in Table 9. While maintaining the profile height, the wavelengths are increased in both simulation approaches.

Variant "1d" follows the approach that the distances in the direction of the feed and the cutting speed are the same and correspond to the derived distance, while the amplitude was reduced by an aspect ratio of AR = 1/4 to A_{US} = 4 µm. However, due to the set wavelength ratio of R_λ = X.0, the kinematic roughness superimposed the oscillation amplitude so that the *Sz* value was also >7 µm. The simulated surface thus exhibits two strong, orthogonal, preferential directions. Therefore, in a second step called "Realistic adaptation", the offset was changed to R_λ = X.5, whereby a peak follows a valley, and this, in conjunction with the implementation of a real measured tool tip (Figure 9), reduced the *Sz* value of the simulation "2d" to just approx. 5 µm.

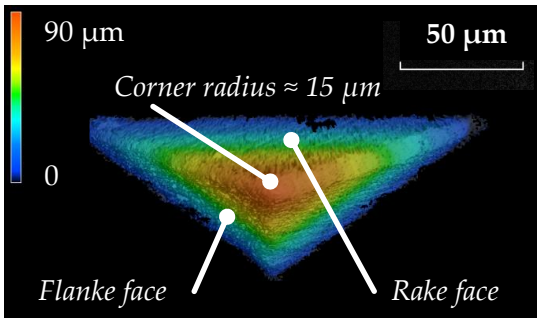

Figure 9. Tool tip in new conditions (HSS).

In variant "1e", an aspect ratio of AR = 1/4 was also chosen for the relation between amplitude and wavelength, but here with the values of A_{US} = 5 µm as well as λ = 20 µm. By means of the wavelength ratio V_λ = X.5 and a modified feed, which corresponded to only half the wavelength (f_z = 10 µm), resulting in circular valleys, so that the surface visually has no preferential direction. In a second adaptation step, the simulation "2e" also used a real 3D cutting geometry of an HSS tool with a tool corner radius of about 15 µm. It is noticeable that this step reverses the visual perception of the surface with "majority peaks" (1d) and "majority valleys" (1e) in both cases.

Table 9. Visual comparison of the variants "d" and "e" of the simulated and via UVSM manufactured surfaces as well as the parameter of the technical adjustment and the conditions of the realistic adaption.

Step	Variant (d)	Variant (e)
Technical adjustment:		
- A_{US}	4 µm	5 µm
- f_z/λ	16 µm/16 µm	10 µm/20 µm
- R_λ	X.0	X.5
Simulation 1	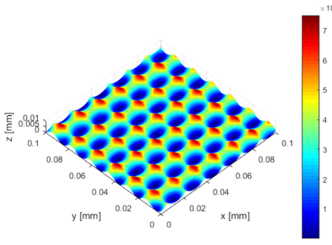	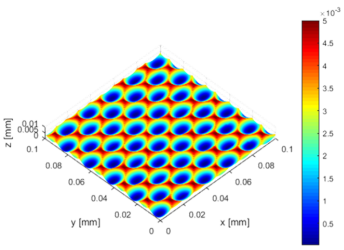
Realistic adaption	Measured cutting tip (HSS, new condition); R_λ = X.5	Measured cutting tip (HSS, new condition)
Simulation 2	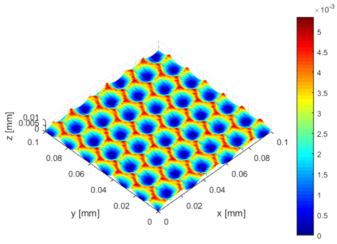	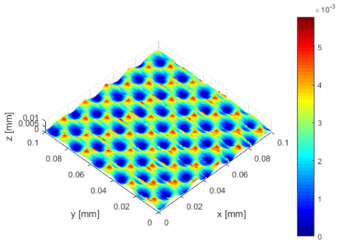
UVSM	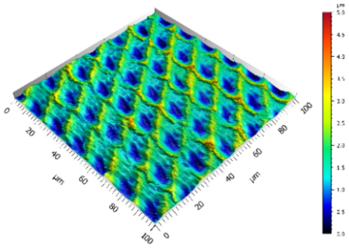	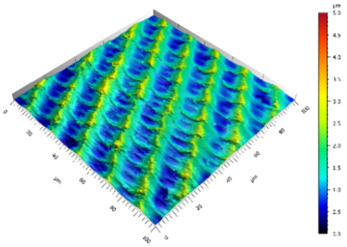

Subsequently, the two simulated combinations (2d and 2e) were experimentally applied to brass specimens using UVSM and with tool inserts with a clearance angle of 40°. HSS was used as the cutting material, since a relatively sharp corner radius of about r_ε = 15 µm could be realized (see Figure 9) as well as sharp cutting edges (cutting edge radius of approximately ≤5 µm). The experimental tests were carried out at the high precision machining centre KERN Pyramid Nano.

In an optical analysis of the surfaces manufactured via UVSM, it was noticeable that there were clearly visible differences as well as similarities to the simulation. Although both surfaces showed visible preferential directions, the individual microstructures in the form of alternating peaks and valleys were just as apparent as the uniform structural distances. However, the profile height in both cases was not as large as in the simulations. A quantitative evaluation, based on the surface parameters selected in Section 3.1, provided further information on the comparability of all surfaces in relation to the particle blasted reference surface. The filter operators "surface aligning" and "Gaussian filter" were disabled for the evaluation of the simulated surfaces, as they are unnecessary for such ideal surfaces without shape deviation or outliers. Furthermore, different values of *Sz* were chosen for the filter of the motif analysis. In some cases, deviations from the standard proposal are useful due to the significance of the elements. The evaluated measuring field size of the simulations as well as the real surfaces was 0.1×0.1 mm^2 in each case. The conditions are summarized in Table 10.

Table 10. Filter conditions for the surface analysis.

Surface	Form Filter	Gaussian Filter	*Sz*-Filter
Particle blasted	✓	✓	5%
Simulation_1d	-	-	5%
Simulation_1e	-	-	5%
Simulation_2d	-	-	10%
Simulation_2e	-	-	10%
UVSM_1d	✓	✓	10%
UVSM_1e	✓	✓	5%

In order to compare all considered surface parameters of the kinematic simulations and the microstructured brass specimen, these were set in relation to the reference averaged values of the blasted sample (Table 5). For this purpose, first the percentage of the reference value was determined, after which the negative as well as positive deviation in the bar chart in Figure 10 can be represented. Accordingly, the closer the percentage deviation is to the (reference) value zero, the more the surfaces are similar in the parameter under consideration.

It is obvious that all values of the motif analysis showed a high accordance with only very small deviations with the reference and, in particular, the value of the surface enlargement *Sdr* showed a good match. In addition, the UVSM_d surface in particular had a comparatively high degree of conformity with the hybrid and feature parameters as well as with the functional parameters, except for *Svk* and Smr1. The already optically observed preferential direction was confirmed by a comparatively low *Str* value, as was the case with UVSM_e and Simulation_1d, while the three remaining surfaces had very high *Str* values and thus were classified as isotropic like the particle-blasted reference surface. This was achieved in particular by a "favorable" ratio R_λ. In the real surfaces, deviations from the default apparently occurred as a result of the process, which influence R_λ and therefore contributed to the strong preferential directions. In addition, because of the progressive tool wear, the corner radius was increased, which resulted in an absence of the valley shape from even troughs. Furthermore, the manufactured microstructures of UVSM_e obtained an analogous value for the root mean square gradient *Sdq*, which showed that they were comparably steep.

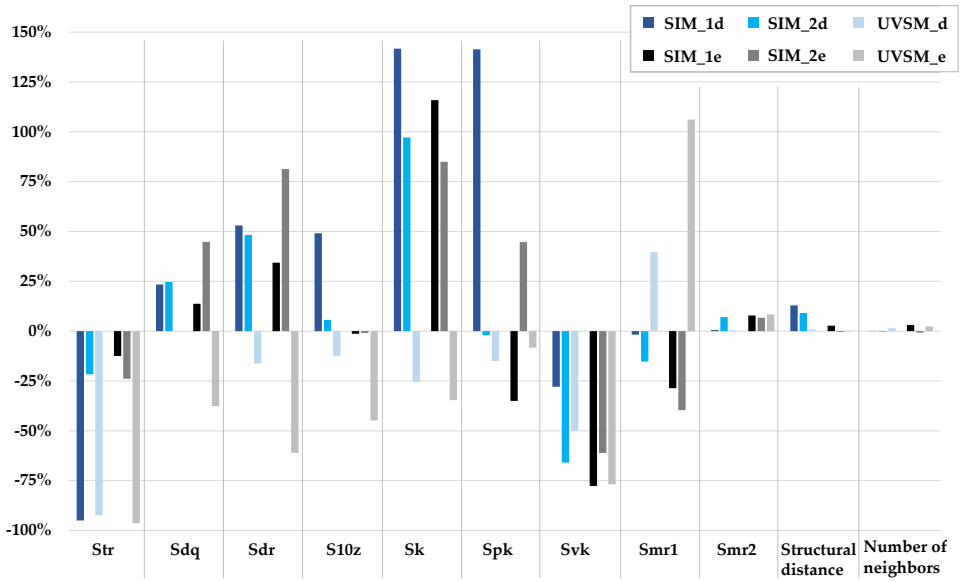

Figure 10. Diagram of all surface parameters of the simulations as well as real manufactured and measured surfaces as a percentage deviation from the respective reference averaged values of the particle blasted surface.

The lower surface magnifications of the surfaces produced in reality are due in particular to their lower profile height. This is illustrated in Figure 11, which shows a cross section in the direction of the cutting speed of the surface UVSM_d. It is noticeable, that the error of UVSM_d was still smaller than UVSM_e. Overall, this variant was significantly closer in most criteria to the requirement profile than UVSM_e, which means that the simulation approach "Variant d" seems more sustainable than "Variant e".

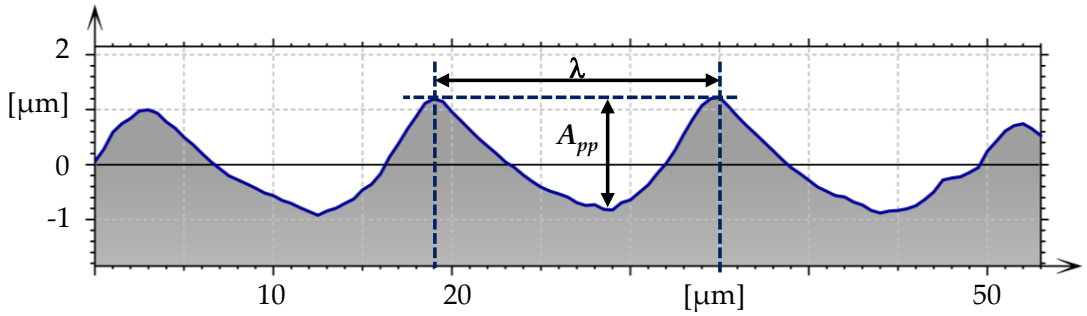

Figure 11. Cross section in the direction of the cutting speed of UVSM_d: λ = 16 µm, A_{pp} = 2 µm.

Particularly prominent is the relatively high consistency of the material and Abbott curves of the manufactured surface UVSM_d with the reference surface (Figure 12). For a comparison, field (c) was chosen. This is noteworthy especially regarding the curves of the two simulated surfaces, which deviated significantly from the "S-shape" of the Abbott curves of the real surfaces. This fact also confirms the quantitative deviation of the functional parameters. Rather, the simulation of the second step shows an almost "linear" behavior of the Abbott curve. This deviation can be considered as a characteristic feature of such simulated, deterministic microstructures. The assumed "ideal" process does not include production-related deviations, like plastic material deformation in the form of burr formation as well as increasing tool wear, and thus also does not form rounded edge areas in the Abbott curve, which represents the presence of peaks, pores, or the like.

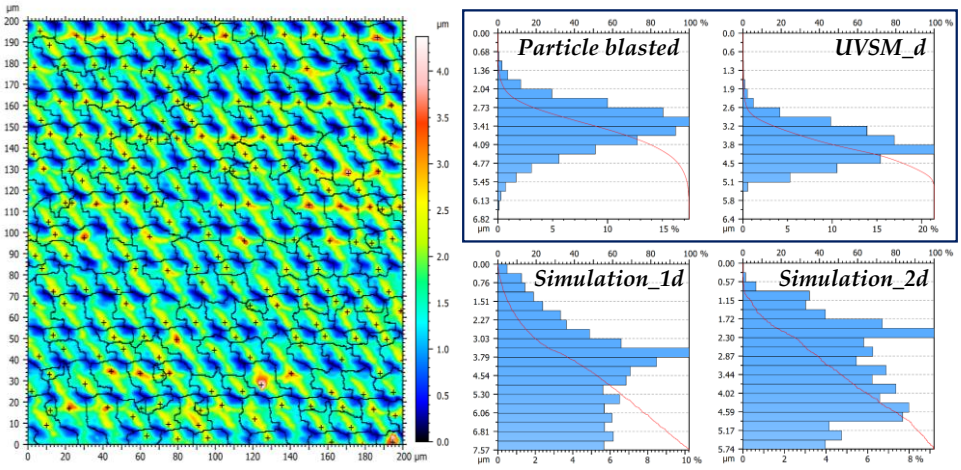

Figure 12. Motif analysis for UVSM_d (**left**) as well as a comparison of the material ratio and the Abbott curves for Variant *d* with the particle blasted curves.

Furthermore, the optical result of the motif analysis is shown in Figure 12. As can be seen, the suitable filter choice of Sz = 10% enabled almost every significant element to be detected, these are defined as peaks of the microstructures. Thus, a sufficient comparability with the particle blasted surface was ensured.

3.4. Tool Wear Behavior

When analyzing the tool wear behavior, it was noticeable that there was no significant difference between the two cutting edges used. Both tools showed a relatively high wear of the cutting edge, in particular on the major cutting edge and the flank face, as shown in Figure 13. On one hand, this is due to the higher mechanical load on the cutting edge in the direction of the feed as well as the instability of the cutting wedge, due to its comparatively small wedge angle. This causes subsequent smoothing of the microstructures, as already described in [16]. Due to the lowered clearance angle as a result of a worn flank face, the *S10z* values of the surfaces or the profile height, respectively, were not as good as in the simulations. In addition, the larger real radius of the cutting corner caused a lower formation of the "valley shape" (see Section 2.2), or as a result, the structural distance in the direction of the feed. Therefore, the tool wear behavior has great influence on the reproducibility of the microstructure and its comparability with the simulation.

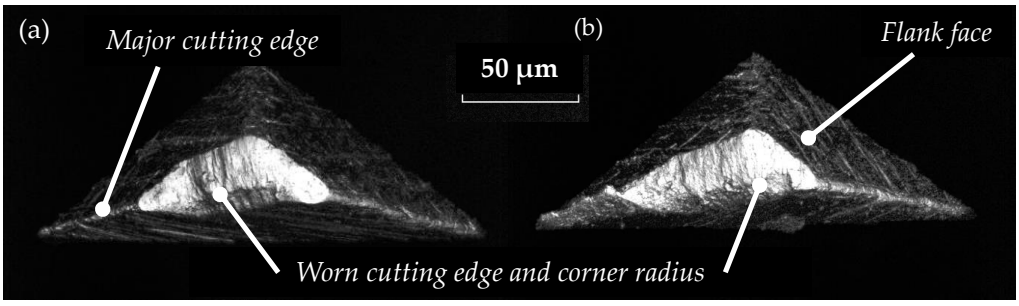

Figure 13. Tool wear on both tools used.

4. Discussion

It could be shown that the derivation of properties of particle blasted surfaces is possible by means of the selection of suitable parameters for the characterization of the surface condition as well as their experimental generation by means of UVSM through a previous kinematic simulation. It turned out that the surface parameters of the motif analysis as well as the spatial, hybrid (only *Sdq*), and feature

parameters are needed particularly to convert these properties and then compare them. One of the reasons for this is that they represent mainly geometrical information. For this reason, they are also suitable for providing information for the design of 2D models for a cooling simulation.

The functional as well as hybrid (only *Sdr*) parameters seemed to only be of limited suitability, as there were considerable differences due to the various characteristics of the surfaces (e.g., in the material distribution). Deviations from the real surfaces from those of the kinematic simulation were due in particular to tool wear and process variations (e.g., within the speed). It might be expedient to use a different cutting material, coated if necessary, in the sense of increasing the reproducibility. However, the preservation of as "sharp" geometries as possible (cutting edge and corner radius) should be taken into account.

The cooling simulation provided initial insights into the expected values of selected residual stress quantities and their behavior in the variation of the as realistic assumed input parameters. However, it became clear that the consideration of the boundary conditions had a decisive importance in the evaluation of these derived trends. An example is the influence of the wavelength on the compressive stresses, which namely decrease with increasing wavelength, but the surface microstructure is thereby approximated to the planar state. This has been proven to be unfavorable for such diamond coatings, since it does not allow elastic stress relaxation and thus a layer thickness of approximately 2 µm is considered critical. Moreover, the use of the correlation factor did not seem to be suitable to adequately characterize each relationship. For example, for only a few input parameters, like the diamond layer thickness with only two values, the correlation factor was comparatively low. However, in a direct comparison of the resulting compressive stresses with otherwise analogous conditions, this had a great influence on the magnitude of the compressive stresses, which was also accompanied by empirical experiences.

In addition, some effects were neglected due to the initially made simplifications, which in reality can be of relevance. For this reason, the provision of further information for the creation of 2D models for a cooling simulation is also suitable.

5. Summary and Conclusions

The ultrasonic vibration superimposed machining is, due to its high design variety or the modification possibilities, respectively, suitable for converting important features of the properties of particle blasted surfaces to a deterministic microstructure. In addition, there is a relatively high degree of conformity of these generated surfaces in numerous relevant surface parameters in comparison to the microstructured surfaces designed by means of a kinematic simulation. Based on these findings, subsequent research work must provide experimental proof that these surfaces, converted into steel specimens, are suitable for adhering diamond layers with a thickness ≥2 µm and thus an increased technological relevance. On one hand, particle blasting with its numerous disadvantages can be substituted. On the other hand, if necessary, even greater layer thicknesses could be achieved, if the hypothesis of elastic bending can be confirmed, possibly in conjunction with further adhesion-enhancing effects such as mechanical interlocking. The validation of the results can be done, for example, by residual stress measurements.

In addition, further iterative steps for the adaptation of the cooling simulation can be performed such as the integration of an intermediate layer including its material-specific properties as well as a conversion into a 3D model of the microstructures.

Furthermore, an increase in the reproducibility of the microstructures or an extension of the aspect ratio should be sought to validate the results of the cooling simulation.

Author Contributions: Conceptualization, R.B.; Methodology, R.B.; Software, M.P. and T.J.; Validation, R.B.; Formal analysis, R.B.; Investigation, R.B.; Resources, A.S.; Data curation, R.B.; Writing—original draft preparation, R.B., M.P., and T.J.; Writing—review and editing, R.B., M.P., and A.S.; Visualization, R.B.; Supervision, A.S.; Project administration, A.S. and R.B.; Funding acquisition, A.S. and R.B.

Funding: This research was funded by the German Research Foundation (Deutsche Forschungsgemeinschaft (DFG, grant number 407169265).

Acknowledgments: The authors gratefully acknowledge the funding of this research by the German Research Foundation (Deutsche Forschungsgemeinschaft, DFG) within the project "Reduction of residual stresses in CVD diamond layers on steel parts through creation of hierarchically structured surface topographies by applying cutting processes".

Conflicts of Interest: The authors declare no conflict of interest. The funders had no role in the design of the study; in the collection, analyses, or interpretation of data; in the writing of the manuscript, or in the decision to publish the results.

Abbreviation

The following abbreviations and symbols are used in this manuscript:

Symbol	Definition
A_1	Amplitude of the substrate microstructure: peak–peak (µm)
A_2	Amplitude of the diamond layer: peak–peak (µm)
A_{fz}	Aspect ratio in the direction of the feed velocity
A_P	Mathematical amplitude (µm)
A_{pp}	Measured ultrasonic amplitude: peak-peak (µm)
AR	Aspect ratio
A_{US}	Ultrasonic amplitude: peak-peak (µm)
CAD	Computer-aided design
CR	Contour mapping ratio
CS	Cooling simulation
CVD	Chemical vapor deposition
D	Diamond layer thickness (µm)
D_{tool}	Tool diameter (mm)
f_{sim}	Sampling rate (s^{-1})
f_{US}	Ultrasonic frequency (kHz)
f_z	Feed per tooth (µm)
HSS	High speed steel
LR	Layer thickness ratio
MR	Material ratio
$M1$	Material of the substrate of a period ($µm^2$)
$M2$	Material of the diamond layer of a period ($µm^2$)
n	Integer
n_{tool}	Rotational speed (min^{-1})
N	Number of intersections per period
$r_{tool,\,eff}$	Effective tool radius (mm)
r_ε	Corner radius (µm)
R_{fz}	Ratio of the feed per tooth in relation to the wavelength of the oscillation
$R_{r\varepsilon}$	Ratio of the corner radius in relation to the wavelength of the oscillation
Rz_{calc}	Maximum possible structure height
R_λ	Ratio of the ultrasonic frequency in relation to the rotational speed
$S10z$	Ten-point height (µm)
Sdq	Root mean square gradient
Sdr	Surface magnification (%)
Sk	Core roughness depth (µm)
$Smr1$	Peak material portion (%)
$Smr2$	Valley material portion (%)
Spk	Reduced peak height (µm)
STL	CAD-file format (Standard Triangulation/Tesselation Language)
Str	Isotropy (%)
Svk	Reduced valley depth (µm)
Sz	Maximum height (µm)

t_{sim}	Minimum temporal resolution (s)
UVSM	Ultrasonic vibration superimposed machining
v_f	Feed velocity (mm/min)
κ	Angle of the major cutting edge (1°)
κ'	Angle of the minor cutting edge (1°)
λ	Wavelength of the oscillation/structural distance in direction of the cutting speed (µm)
$\sigma_{\mu\nu}$	Minimum principal stress (GPa)
ΔXY	Distance of neighboring dexels in X and Y direction (µm)
$\Delta\sigma_{compression}$	(absolute) Difference of the compressive stresses (GPa)

Appendix A

Appendix A: Result list of the cooling simulation taking into account all considered combinations of input parameters.

References

1. Amaral, M.; Almeida, F.; Fernandes, A.; Costa, F.; Oliveira, F.; Silva, R.; Costa, F.; Oliveira, F. The role of surface activation prior to seeding on CVD diamond adhesion. *Surf. Coat. Technol.* **2010**, *204*, 3585–3591. [CrossRef]
2. Singh, R.K.; Gilbert, D.R.; Fitz-Gerald, J.; Harkness, S.; Lee, D.G. Engineered Interfaces for Adherent Diamond Coatings on Large Thermal-Expansion Coefficient Mismatched Substrates. *Science* **1996**, *272*, 396–398. [CrossRef]
3. Wako, H.; Abe, T.; Takagi, T.; Ikohagi, T. Comparison of diamond film adhesion on molybdenum substrates with different surface morphologies. *Appl. Surf. Sci.* **2009**, *256*, 1466–1471. [CrossRef]
4. Xu, Z.; Lev, L.; Lukitsch, M.; Kumar, A. Effects of surface pretreatments on the deposition of adherent diamond coatings on cemented tungsten carbide substrates. *Diam. Relat. Mater.* **2017**, *16*, 461–466. [CrossRef]
5. Gomez, H.; Durham, D.; Xiao, X.; Lukitsch, M.; Lu, P.; Chou, K.; Sachdev, A.; Kumar, A. Adhesion analysis and dry machining performance of CVD diamond coatings deposited on surface modified WC-Co turning inserts. *J. Mater. Process. Technol.* **2012**, *212*, 523–533. [CrossRef]
6. Lee, D.; Gilbert, D.; Lee, S.; Singh, R. Surface composites: A novel method to fabricate adherent interfaces in thermal-mismatched systems. *Compos. Part B Eng.* **1999**, *30*, 667–674. [CrossRef]
7. Grögler, T.; Zeiler, E.; Horner, A.; Rosiwal, S.; Singer, R. Microwave-plasma-CVD of diamond coatings onto titanium and titanium alloys. *Surf. Coat. Technol.* **1998**, *98*, 1079–1091. [CrossRef]
8. Grögler, T.; Franz, A.; Klaffke, D.; Rosiwal, S.M.; Singer, R.F. Tribological optimization of CVD diamond coated Ti-6Al-4V1. *Diam. Relat. Mater.* **1998**, *7*, 1342–1347. [CrossRef]
9. Grögler, T.; Plewa, O.; Rosiwal, S.; Singer, R. CVD diamond films as protective coatings on titanium alloys. *Int. J. Refract. Met. Hard Mater.* **1998**, *16*, 217–222. [CrossRef]
10. Zeiler, E.; Klaffke, D.; Hiltner, K.; Grögler, T.; Rosiwal, S.; Singer, R. Tribological performance of mechanically lapped chemical vapor deposited diamond coatings. *Surf. Coat. Technol.* **1999**, *116*, 599–608. [CrossRef]
11. Lim, P.; Lin, F.; Shih, H.; Ralchenko, V.; Varnin, V.; Pleskov, Y.; Hsu, S.; Chou, S.; Hsu, P. Improved stability of titanium based boron-doped chemical vapor deposited diamond thin-film electrode by modifying titanium substrate surface. *Thin Solid Films* **2008**, *516*, 6125–6132. [CrossRef]
12. Damm, D.D.; Contin, A.; Barbieri, F.C.; Trava-Airoldi, V.J.; Barquete, D.M.; Corat, E.J. Interlayers Applied to CVD Diamond Deposition on Steel Substrate: A Review. *Coatings* **2017**, *7*, 141. [CrossRef]
13. Seewig, J.; Wiehr, C.; Gröger, S. *Charakterisierung Technischer Bauteiloberflächen, Arbeitskreis 3D-Rauheitsmesstechnik*; VDI Wissensforum GmbH: Düsseldorf, Germany, 2012.
14. Leach, R. *Characterisation of Areal Surface Texture*; Springer: Berlin/Heidelberg, Germany, 2013.
15. Hartmann, W.D. Mess- und Auswertestrategien zur Modellbasierten Bewertung Funktionaler Eigenschaften Mikrostrukturierter Oberflächen. Ph.D. Thesis, Friedrich-Alexander-Universität, Erlangen, Germany, 2014.
16. Börner, R.; Winkler, S.; Junge, T.; Titsch, C.; Schubert, A.; Drossel, W.-G. Generation of functional surfaces by using a simulation tool for surface prediction and micro structuring of cold-working steel with ultrasonic vibration assisted face milling. *J. Mater. Process. Technol.* **2018**, *255*, 749–759. [CrossRef]

17. Prieske, M.; Börner, R.; Schubert, A. Influence of the surface microstructure on the adhesion of a CVD-diamond coating on steel with a CrN interlayer. *MATEC Web Conf.* **2018**, *190*, 14008. [CrossRef]
18. Kellermann, K.; Bareiß, C.; Rosiwal, S.M.; Singer, R.F. Well Adherent Diamond Coatings on Steel Substrates. *Adv. Eng. Mater.* **2008**, *10*, 657–660. [CrossRef]